

Tunable Quantum Beat of Single Photons Enabled by Nonlinear Nanophotonics

Qing Li,^{1,2,3,*} Anshuman Singh,^{1,2} Xiyuan Lu,^{1,2} John Lawall,¹ Varun Verma,⁴ Richard Mirin,⁴ Sae Woo Nam,⁴ and Kartik Srinivasan^{1,5,†}

¹*Physical Measurement Laboratory, National Institute of Standards and Technology, Gaithersburg, Maryland 20899, USA*

²*Institute for Research in Electronics and Applied Physics and Maryland Nanocenter, University of Maryland, College Park, Maryland 20742, USA*

³*Department of Electrical and Computer Engineering, Carnegie Mellon University, Pittsburgh, Pennsylvania 15213, USA*

⁴*Physical Measurement Laboratory, National Institute of Standards and Technology, Boulder, Colorado 80305, USA*

⁵*Joint Quantum Institute, NIST/University of Maryland, College Park, Maryland 20742, USA*



(Received 5 May 2019; revised manuscript received 19 August 2019; published 22 November 2019)

We demonstrate the tunable quantum beat of single photons through the co-development of core nonlinear nanophotonic technologies for frequency-domain manipulation of quantum states in a common physical platform. Spontaneous four-wave mixing in a nonlinear resonator is used to produce nondegenerate, quantum-correlated photon pairs. One photon from each pair is then frequency shifted, without degradation of photon statistics, using four-wave-mixing Bragg scattering in a second nonlinear resonator. Fine tuning of the applied frequency shift enables tunable quantum interference of the two photons as they are impinged on a beam splitter, with an oscillating signature that depends on their frequency difference. Our work showcases the potential of nonlinear nanophotonic devices as a valuable resource for photonic quantum-information science.

DOI: [10.1103/PhysRevApplied.12.054054](https://doi.org/10.1103/PhysRevApplied.12.054054)

I. INTRODUCTION

Frequency-bin-encoded states have attracted significant interest in quantum-information processing due to the ease in realizing high-dimensional entanglement [1–3]. This approach is particularly attractive in terms of resource scaling for chip-scale implementations. However, to fully explore such scalability, many physical resources need to be designed and reinvented using nanophotonics technology. For example, cross-modal coupling between frequency bins requires active elements that can efficiently provide controllable frequency shifts. Here, we demonstrate how silicon nanophotonics can support essential nonlinear nanophotonic technologies—quantum light generation and quantum frequency conversion—to underpin such research.

In particular, we demonstrate the key ability to flexibly tailor $\chi^{(3)}$ nonlinear interactions to realize these two distinct quantum photonic functionalities within a common device platform (Fig. 1). Specifically, the quantum source uses spontaneous four-wave mixing (SFWM) in a stoichiometric silicon nitride (Si_3N_4) microring resonator

to produce temporally correlated photon pairs [4], while quantum frequency conversion (QFC) is implemented through four-wave-mixing Bragg scattering (FWM BS) [5] in a similar Si_3N_4 microring [6,7]. The successful combination of photon-pair generation and frequency conversion using a common platform enables demonstration of frequency conversion of a quantum state of light and establishes its relevance to frequency-bin-encoded quantum photonics [1–3,8]. Here, the inherent high dimensionality in which photon pairs are distributed amongst frequency modes necessitates methods to implement controllable frequency shifts that enable efficient mixing of frequency bins. To that end, we use QFC to remove the spectral distinguishability between the two nondegenerate photons comprising a photon pair, and demonstrate tunable Hong-Ou-Mandel interference in which the quantum beat of single photons is observed [9].

II. SYSTEM OVERVIEW

Figure 1 provides a schematic overview in which one photon from a nondegenerate microresonator photon-pair source is sent to a microresonator frequency converter. An important distinguishing aspect of our work is its focus on achieving both quantum light generation and QFC [10,11]

*qingli2@andrew.cmu.edu

†kartiks@umd.edu

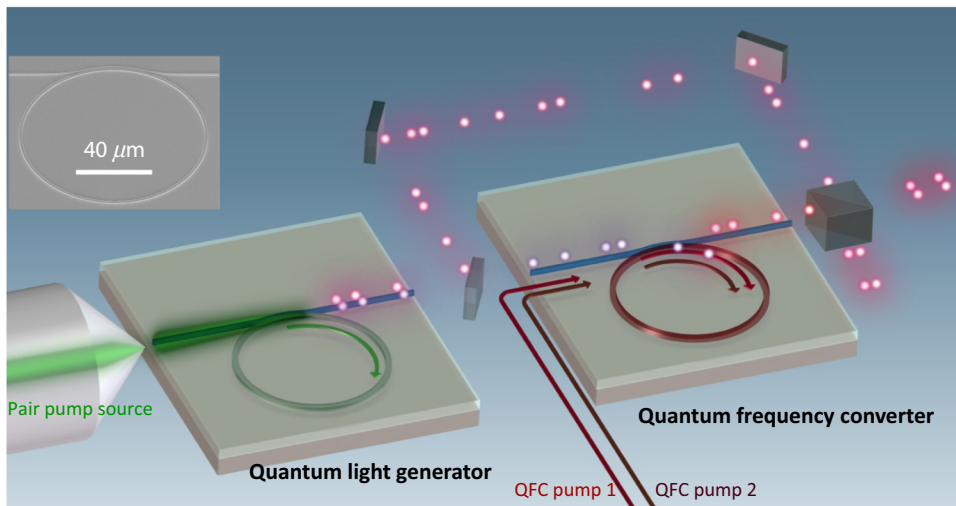


FIG. 1. Quantum beats using nonlinear nanophotonics. Photon pairs are generated by spontaneous four-wave mixing in a Si_3N_4 microring. The signal photon is sent to the frequency converter, where it is spectrally translated to the vicinity of the idler frequency through four-wave-mixing Bragg scattering in a second Si_3N_4 microring. A tunable quantum beat is observed in the Hong-Ou-Mandel interference of the idler and the frequency-converted signal, with a signature that depends on their frequency difference.

within a common platform based on chip-integrated silicon nanophotonics. This stands in contrast to existing demonstrations, where centimeter-scale nonlinear crystals or meter-scale optical fibers [12–26] are used to achieve QFC of a variety of sources, ranging from probabilistic sources based on nonlinear optics in crystals and fibers [14,18,23] to on-demand sources based on single quantum emitters such as quantum dots [15,16,26], trapped ions and neutral atoms [22,25], and nitrogen-vacancy centers in diamond [24]. Very recently, we have used a nanophotonic QFC chip to operate on a single-photon source based on a single quantum dot in a micropillar cavity at cryogenic temperatures [7]. Our work here is distinguished from that study, both by establishing the two quantum resources within the same physical system operating at room temperature, and also by demonstrating the use of nanophotonic QFC to enable tunable quantum interference of single photons.

Achieving efficient $\chi^{(3)}$ nonlinear processes in microresonators [27] requires phase and frequency matching of the four involved fields, as well as efficient injection and extraction from the resonators at the signal, idler, and pump wavelengths. To integrate nanophotonic elements based on different nonlinear processes, these criteria must be simultaneously satisfied for each element, while ensuring that the device geometries are compatible. The Si_3N_4 microring we optimize for FWM BS shows small normal dispersion in both the 930- and 1550-nm bands (Appendix A). As a result, photon pairs can be generated in microrings of similar dimensions (most critically, the same device layer thickness), by simply pumping with a relatively strong power (mW level) in either of these two near-zero dispersion bands, with SFWM resulting in annihilation of two pump photons and creation of a quantum-correlated signal and idler pair. Because the photon-pair source and frequency converter are implemented in rings with the same device layer thickness, they

can be naturally integrated on the same chip, ideally with filters, phase shifters, detectors, and other photonic elements, many of which have been demonstrated in Si_3N_4 [28–31]. To retain flexibility in independent characterization of the source and frequency converter, here they are on separate chips, but there is no significant barrier to future direct integration.

III. DEVICES

The photon-pair source is implemented in 40- μm radius, 500-nm-thick Si_3N_4 microrings with ring widths around 1500 nm (Fig. 1). Due to the aforementioned small dispersion in the 930-nm band, we expect to observe a quantum comb consisting of a number of signal and idler frequency bins, as illustrated in Fig. 2(a) and experimentally observed in Fig. 2(b). While such a quantum comb can exhibit high-dimensional entanglement across these frequency bins [2], here we work with one signal-idler combination at a given time [highlighted in Fig. 2(b)], through pump rejection and bandpass filters. We perform quantum-source characterization by passively transmitting the signal photons through the subsequent frequency-converter chip (i.e., without applying the pumps that enable frequency conversion) and then onto a single-photon detector, while the idler photons are directly sent to a second single-photon detector, with the photon flux and signal-idler coincidences recorded (see Appendix D and Fig. 10 for the experimental setup schematic). As shown in Fig. 2(b), the detected signal photon flux is approximately equal to $3.6 \times 10^5 \text{ s}^{-1}$ for a pump power approximately equal to 4 mW, while the on-chip pair-generation rate is approximately equal to $2 \times 10^7 \text{ s}^{-1}$ after accounting for losses. We further characterize the quantum source by measuring its linewidth to be approximately equal to 640 MHz, and characterizing its coincidence-to-accidental ratio (CAR), defined as the ratio between the peak coincidence contrast and noise

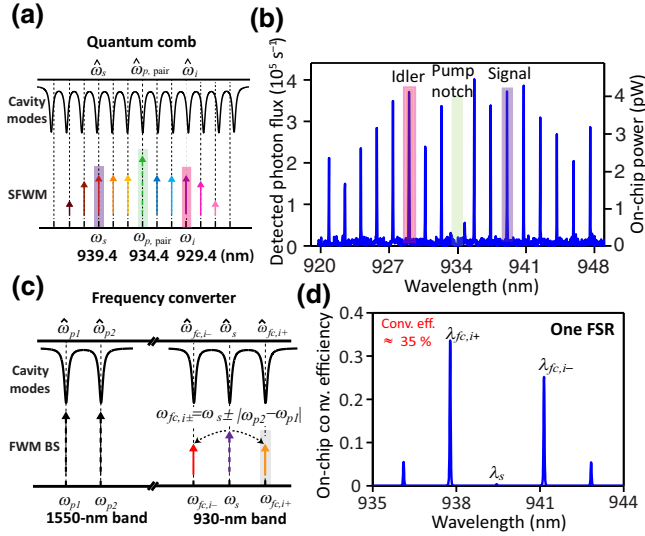


FIG. 2. Microresonator photon-pair source and frequency converter. (a) Schematic of the SFWM process in a Si₃N₄ microring, where quantum-correlated signal and idler photons are distributed amongst multiple frequency bins. (b) Measured pair spectrum for an input power near 4 mW, where the left y axis is the detected signal photon flux and the right y axis is the corresponding on-chip power. The highlighted third-order pair in (a) and (b) is chosen as the signal and idler for the quantum frequency conversion experiment demonstrated in Fig. 3. (c) Schematic of the intraband conversion scheme based on FWM BS, where the signal is translated to nearby resonances with the frequency shift determined by the frequency difference of two pump lasers in the 1550-nm band. (d) Output spectrum of the frequency converter with one free spectral range (FSR) separation between the two pump lasers (frequency translation approximately equal to 572 GHz) for a total pump power of 20 mW on chip (10 mW each). The power in the 930-nm band is normalized by the input signal power. The input signal in this case is a narrow linewidth, cw laser.

background, as a function of pump power. The CAR corresponding to Fig. 2(b) is approximately equal to 10 (more details provided in Appendix B). Although these CAR values are considerably lower than the best achieved in Si₃N₄ resonators when very widely separated photon pairs were generated [32] and in Si microresonators [33], they are comparable to other intraband pair sources based on microrings in Si₃N₄ and similar materials [34,35].

The frequency converter is based on FWM BS in a 40- μ m radius, 500-nm-thick Si₃N₄ microring with 1450-nm ring width. In FWM BS, the spectral shift is set by the difference in frequencies of the two applied pumps [5]. We focus on intraband translation due to its specific relevance to quantum-comb sources. Here, the two pumps are on resonance with cavity modes in the 1550-nm band (cavity FSR is 0.57 THz), with input signal photons in the 930-nm band [Fig. 2(c)]. By optimizing the device performance, we observe that for an input signal

with bandwidth much smaller than the cavity linewidth (in this case, a cw laser < 200 kHz linewidth), the signal can be completely depleted [Fig. 2(d)]. The first-order blue-shifted idler ($fc, i+$) has an on-chip conversion efficiency around 35%, whereas the conversion efficiency of the first-order red-shifted idler ($fc, i-$) is around 25%. This asymmetry arises from the slight frequency mismatch between the amount of frequency shift (determined by the pump separation) and the FSR in the 930-nm band, and can be used to enhance the power of one particular idler (the example of the red idler being stronger than the blue is shown later in the quantum-beat experiment; see Fig. 13(b)). Second-order idlers are also observed, but with significantly reduced conversion efficiency. A systematic investigation of conversion efficiency, bandwidth, asymmetric idler conversion efficiency, and on-chip noise as a function of the pump power is presented in Appendix C.

IV. QUANTUM FREQUENCY CONVERSION

We next consider the combined operation of the quantum light source and frequency converter. The frequency converter is operated at a total applied pump power of 20 mW, corresponding to a 2-GHz converter bandwidth and 3-fW on-chip noise. This provides adequate conversion bandwidth (compared to the pair-source bandwidth of 640 MHz) while maintaining sufficiently low noise. Adjusting the frequency-converter temperature enables spectral matching of its relevant mode to the pair-source signal photon (at $\lambda_s \approx 939$ nm). Figure 3(a) shows the output spectrum corresponding to one-FSR frequency translation, where the remnant photon-pair-source signal is several times smaller than the two frequency-converted idlers. Its suppression is weaker than the cw case [Fig. 2(d)] due to its much broader linewidth, which is an appreciable fraction of the 2-GHz conversion bandwidth. For the same reason, the conversion efficiency of the blue idler has degraded from 35% in the cw case to 25%, which is expected given the input signal bandwidth (detailed analysis in Appendix C). Nevertheless, we note that the conversion efficiency achieved in this work is quite similar to the 28% efficiency achieved in the first demonstration of QFC using FWM BS [14].

Figure 3(b) shows a high-resolution spectrum of the frequency-converted blue idler [highlighted in Fig. 3(a)], displaying essentially the same bandwidth as the original pair-source signal. In addition, a weak resonance-shaped noise peak at the same frequency as the blue idler is detected by blocking the input signal but continuing to apply the frequency-converter pumps. This noise is also observable in the broad spectrum shown in Fig. 3(a) (i.e., the small peaks at the longest wavelengths). In Fig. 3(c), the CAR after conversion (red curve), which correlates the frequency-converted idler and the original pair-source

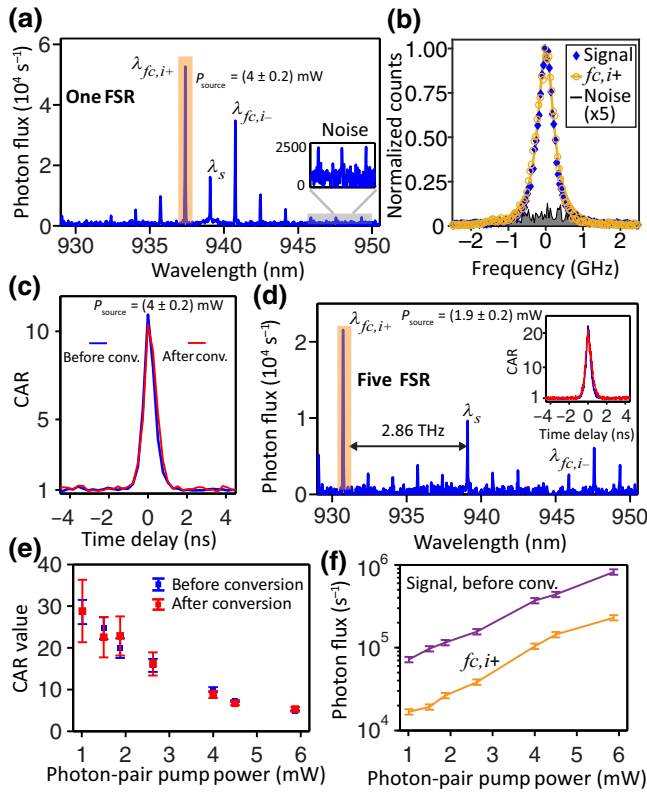


FIG. 3. Quantum frequency conversion. (a) Frequency-converted spectrum in which the signal photons from the photon-pair source [see Fig. 2(b)] are spectrally translated with one-FSR pump separation. The inset shows an enlargement plot of the resonant noise induced by the two 1550-nm pumps. (b) High-resolution spectra of the input signal, frequency-converted blue idler highlighted in (a), and resonant noise. The resonant noise is detected by removing the input signal. It shares a common normalization with the frequency-converted blue idler, and is enlarged five times in the plot for clarity. (c) Measured CAR values corresponding to (a). The blue curve is taken for the pair-source signal and idler before conversion, while the red curve is for the frequency-converted blue idler and original pair-source idler. (d) Spectrum for five-FSR frequency separation and a reduced photon-pair-source flux (pumped at 1.9 mW instead of 4 mW). The inset shows the corresponding CAR values before (blue) and after (red) conversion. (e) Comparisons of CAR values before and after conversion as a function of photon-pair-source pump power. (f) Detected flux of the pair-source signal photons before conversion and the frequency-converted blue idler photons after conversion [one-FSR shift as in (a)]. The on-chip conversion efficiency is estimated to be $25\% \pm 3\%$. The converted photon flux is corrected to account for the 50% loss from the bandpass filter used to select the blue idler.

idler, is compared against the CAR before conversion (blue curve). The almost identical responses suggest that the additional noise introduced in the QFC process is small relative to the signal level. In Fig. 3(d), we increase the frequency separation between the two pumps to five FSRs, and a similar conversion efficiency near 25% is obtained

for the corresponding five-FSR-shifted blue idler. Compared to Fig. 3(a), the pump power for the photon-pair source is reduced, resulting in a smaller photon flux but an increased CAR near 20 both before and after conversion [inset in Fig. 3(d)]. Finally, a scan of the pump power for the photon-pair source is performed while keeping the configuration of the frequency converter fixed. The results, shown in Fig. 3(e), demonstrate that the quantum correlation between the photons in the pair source are preserved by our frequency converter (within the measurement error), with a uniform conversion efficiency $25\% \pm 3\%$ [Fig. 3(f)] for the full range of input photon flux. Additional analysis of noise in the QFC process is presented in Appendix E.

V. QUANTUM BEAT OF SINGLE PHOTONS

Having demonstrated QFC, here we use it to observe the tunable quantum beat of single photons. This is accomplished by using a photon-pair source whose FSR is nearly the same as that of the frequency converter. The experimental scheme is illustrated in Fig. 4(a), where the photon-pair-source signal and idler are initially separated by two FSRs (approximately equal to 1.14 THz). The signal photons are then brought spectrally close to idler photons through QFC. While the frequency-converter FSR largely determines this spectral shift, fine tuning can be achieved because the cavity modes have a finite linewidth. That is, we can tune the pump lasers within their respective cavity-mode linewidths (few hundred MHz each) to achieve the precise spectral shift needed for high-visibility interference (Appendix F).

Figure 4(b) confirms that for an optimized frequency shift, the original pair-source idler and the frequency-converted red idler spectrally overlap (i.e., $\Delta f = 0$). Since these two photons are nearly identical and strongly correlated in time, we can send them to a 50:50 fiber coupler and perform a two-photon interference experiment. First, we ensure that two photons arrive at the coupler at the same time through a tunable optical delay line [Fig. 4(a)]. By adjusting the polarization of the pair-source idler photon while fixing that of the frequency-converted idler, two distinct responses in the coincidence measurement are observed. If the two photons are orthogonally polarized [blue curve in Fig. 4(c)], we observe a coincidence peak whose CAR value is half what it was before entering the 50:50 coupler [inset to Fig. 4(c)]. On the other hand, if we adjust their polarization to be the same, the coincidence peak disappears to the background accidental coincidence level [red curve in Fig. 4(c)], indicating destructive interference. Essentially, there are two possibilities corresponding to the detection of one photon at each detector: each photon exits from its through port of the coupler, or each photon exits from its cross port. The probability amplitudes associated with these two scenarios

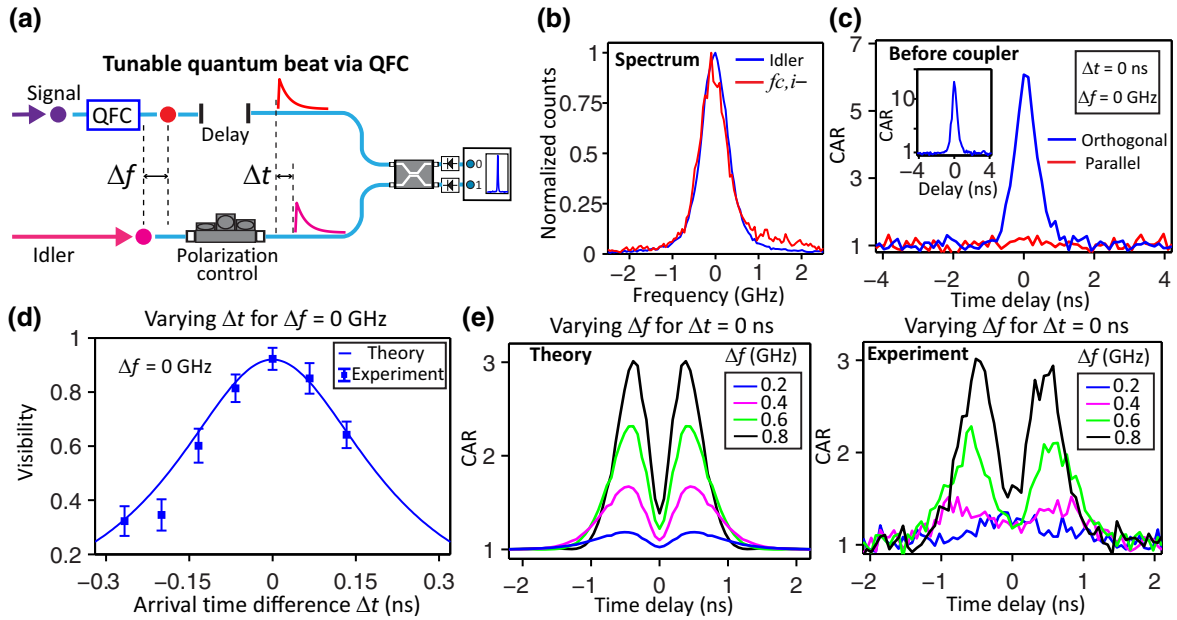


FIG. 4. Tunable quantum beat enabled by QFC. (a) Experimental schematic, where the frequency difference of the two photons (Δf), the relative arrival time on the coupler (Δt), and the relative polarization can all be varied. (b) Superimposed high-resolution spectra for the pair-source idler and the frequency-converted idler. (c) Coincidence counting after the 50:50 coupler, taken for $\Delta t = 0$ and $\Delta f = 0$, for both orthogonal (blue) and parallel (red) polarizations. The inset shows the coincidence counting measurement for the two photons before entering the 50:50 coupler. (d) Theoretical (solid curve) and measured (markers with error bars) visibility as a function of the relative optical delay between two photons, with $\Delta f = 0$. (e) Theoretical (left) and experimental (right) coincidence counting corresponding to $\Delta t = 0$ and varied frequency difference (Δf). Only the co-polarized case is considered in (e).

cancel, resulting in an accidental-level coincidence rate, i.e., the Hong-Ou-Mandel effect [36].

Next, we vary the frequency difference (Δf) and the relative optical delay (Δt) between the pair-source idler and the frequency-converted idler. In the first case, the two photons share the same frequency but arrive at the 50:50 coupler at different times (i.e., $\Delta t \neq 0$ and $\Delta f = 0$). To characterize this process, we define a visibility based on the contrast of peak values in the coincidence rate between the parallel and orthogonal polarizations. The experimental data [Fig. 4(d)], showing a maximum visibility $> 90\%$, agrees with the simulation result reasonably well (see Appendix G for theoretical modeling). In the second case, where the two photons arrive at the coupler at the same time but with different frequencies (i.e., $\Delta t = 0$ and $\Delta f \neq 0$), the normalized coincidence rate (by the orthogonal polarization case) for the parallel polarization is given by $1 - \cos(2\pi \Delta f \tau)$, where τ is the relative electronic delay between the two detectors [i.e., the x axis in Fig. 4(e)]. This formula indicates that even if the two photons have different frequencies, there is an interference dip at $\tau = 0$, which is confirmed by experimental results shown in Fig. 4(e). As can be seen, the interference dip fails to reach the accidental coincidence level for large Δf , which is mainly due to the limited detector timing resolution (120 ps) and time bin (64 ps) used in the coincidence counting. After taking these factors into consideration, a

reasonable agreement between theory and experiment is observed. Oscillations in the two-photon interference of single photons with slightly different frequencies has been referred to as a quantum beat [9], and shows the sensitivity of two-photon interference to precise spectral matching [37]. One can thus use the quantum-beat phenomenon as a technique to diagnose how precisely initially nondegenerate photons are brought into spectral alignment via QFC.

VI. SUMMARY

We thus demonstrate the generation and frequency conversion of quantum states of light in a nonlinear nanophotonic platform. The high-visibility and controllable-frequency differences achieved indicate that nanophotonic QFC could become an enabling technology for realizing the high-quality quantum interference needed for various applications. In such situations, the quantum beat observed when interfering photons that are slightly detuned serves as a sensitive probe for determining how the QFC process should be tuned to realize precise spectral matching. Going forward, the frequency-bin-entangled states produced by microresonator SFWM and their synergy with QFC makes the platform appealing for exploring sophisticated frequency-domain manipulation of quantum states. Operation of the FWM BS device as a frequency

tritter [38] and as a nonlinear element addressing all frequency bins simultaneously are amongst the opportunities enabled by our platform.

ACKNOWLEDGMENTS

Q.L., A.S., and X.L. acknowledge support under the Cooperative Research Agreement between the University of Maryland and NIST Physical Measurement Laboratory, Award 70NANB14H209. The authors wish to thank Marcelo Davanço from NIST Gaithersburg and Abijith Kowli from NIST Boulder for helpful comments.

APPENDIX A: LINEAR TRANSMISSION AND DISPERSION CHARACTERIZATION

The 40- μm radius Si_3N_4 microring resonators employed in this work, both for the photon-pair generation and frequency conversion, are similar to the ones adopted in our earlier work [6]. The Si_3N_4 thickness is around 500 nm, and the ring width is varied from 1400 to 1600 nm with a step size of 10 nm. The coupling between the resonator and access waveguide is based on a pulley coupling scheme, which can be engineered by varying the access waveguide width, gap, and pulley coupling length. Optimization of these parameters allows us to tailor the properties of

microring resonators, in terms of their FSR, dispersion, and coupling, for each specific application. For example, there are two essential requirements for intraband frequency conversion in the 930-nm band: (1) identical FSRs between the 1550- and 930-nm bands to satisfy frequency matching (for modes that are phase matched), and (2) overcoupling of the resonances in the 930-nm band to attain overall high conversion efficiencies. In addition, the resonances in the 1550-nm band are preferred to be critically coupled so the required pump powers are minimized.

The transmission of a typical microring resonator, both in the 930- and 1550-nm bands, is provided in Fig. 5. The resonance frequencies in each band can be approximated by the Taylor series $\hat{\omega}_\mu = \hat{\omega}_0 + D_1\mu + \frac{1}{2}D_2\mu^2 + \dots$, where $\hat{\omega}_0$ is the reference frequency, $D_1/2\pi$ is the FSR of the resonator at $\hat{\omega}_0$, D_2 is the quadratic dispersion, and μ is an integer representing the relative mode-order number with respect to $\hat{\omega}_0$. As shown in Fig. 5, the dispersion in both bands is found to be normal ($D_2 < 0$) and small enough to enable photon-pair generation in either band by simply pumping the resonance at a relatively high power. While the resonances in the 930-nm band of this representative device are overcoupled to achieve high conversion efficiencies for the frequency-conversion process, for the photon-pair generation we use a slightly

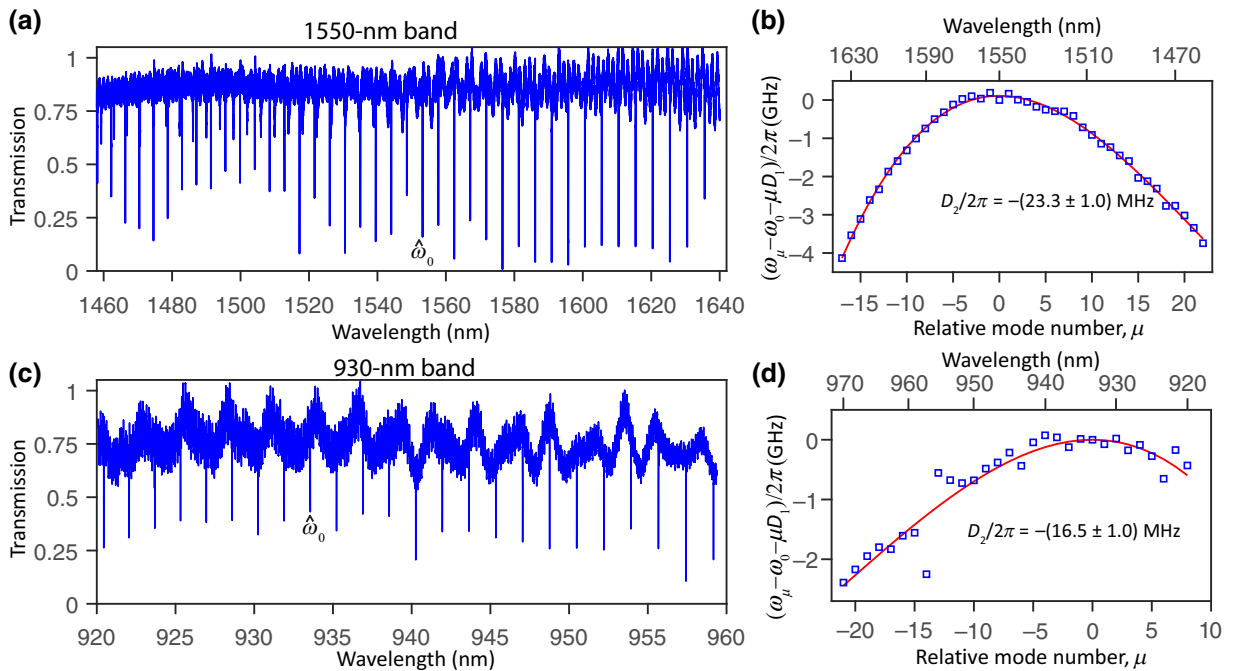


FIG. 5. Linear transmission and dispersion of a representative Si_3N_4 microring. (a) Linear transmission scan of a representative device (used as the frequency converter in this work) in the 1550-nm band, where $\hat{\omega}_0$ marks the reference frequency for dispersion determination. (b) Deviation of the measured resonance frequencies (markers) from an equidistant frequency grid $\hat{\omega}_0 + \mu D_1$ in the 1550-nm band. The extracted D_2 is provided, where the displayed one standard deviation uncertainty is determined from a nonlinear least-squares fit to the data. (c) Linear transmission scan of the same device as (a) in the 930-nm band, where the resonances are overcoupled to achieve high conversion efficiencies. (d) Deviation of the measured resonance frequencies (markers) from an equidistant frequency grid $\hat{\omega}_0 + \mu D_1$ in the 930-nm band. Coupling between the mode of interest and another mode of the resonator at $\mu \approx -13$ causes a deviation from quadratic behavior; these points are not included in the fit.

modified waveguide-resonator coupling design, choosing it to be near critical coupling in the 930-nm band. This ensures that the spectral bandwidth of the emitted photon pairs is several times smaller than the frequency-conversion bandwidth.

APPENDIX B: PHOTON-PAIR-SOURCE CHARACTERIZATION

As shown in Fig. 6(a), the resonances for the photon-pair generation microring in the 930-nm band are critically coupled with a loaded quality factor $Q \approx 5 \times 10^5$ in the linear regime. This corresponds to a spectral bandwidth approximately equal to 640 MHz, consistent with the result from the scanning Fabry-Perot measurement [see Fig. 3(b) in the main text]. With increased pump powers, the resonator starts to generate an appreciable photon-pair flux while eventually exhibiting thermal bistability in the pump transmission. In Fig. 6(b), we plot the detected signal (or idler) photon flux (right y axis) as a function of the pump power, from which the on-chip pair-generation rate is estimated after accounting for various losses in the transmission link [see the inset shown in Fig. 6(b)]. Subsequently, the CAR for the selected signal and idler pair is measured [red solid line in Fig. 6(c)], which has a peak value around 70 at a pump power near 0.67 mW. We also plot the CAR measurement by transmitting the signal through the frequency-conversion chip without applying any pumps [blue markers in Fig. 6(c), corresponding to the “before conversion” case shown in Fig. 3(e) in the main text]. As can be seen, the additional loss in the signal and

idler photons incurred from passing through the frequency converter does not degrade the CAR value much for the range of pump power tested. A more detailed study analyzing the impact of various noise sources (including the Raman noise) on the CAR measurement is provided later in Appendix E.

APPENDIX C: FREQUENCY CONVERTER: ADDITIONAL DISCUSSION

1. Characterization

The frequency-converter devices are initially characterized using a narrow linewidth, cw laser for the input signal. Figure 7(a) shows the signal resonance for three different pump powers, going from the overcoupled regime at low pump powers to the critically coupled and undercoupled regimes at increased pump powers, as the input signal is depleted due to frequency conversion into output idlers. The width of the signal resonance also increases with increasing pump power, indicating that the conversion bandwidth can be broadened beyond the microresonator’s loaded linewidth in the linear regime. The spectra of one-FSR separation and five-FSR separation are provided in Figs. 7(b) and 7(c), respectively, showing a consistent conversion efficiency above 35% for the blue idler.

The pump-power dependence of the conversion efficiency, bandwidth, and generated noise power are shown in Figs. 7(d)–7(f), respectively. As can be seen in Fig. 7(d), the conversion efficiency saturates at $30\% \pm 5\%$ for total pump powers above 10 mW. However, both

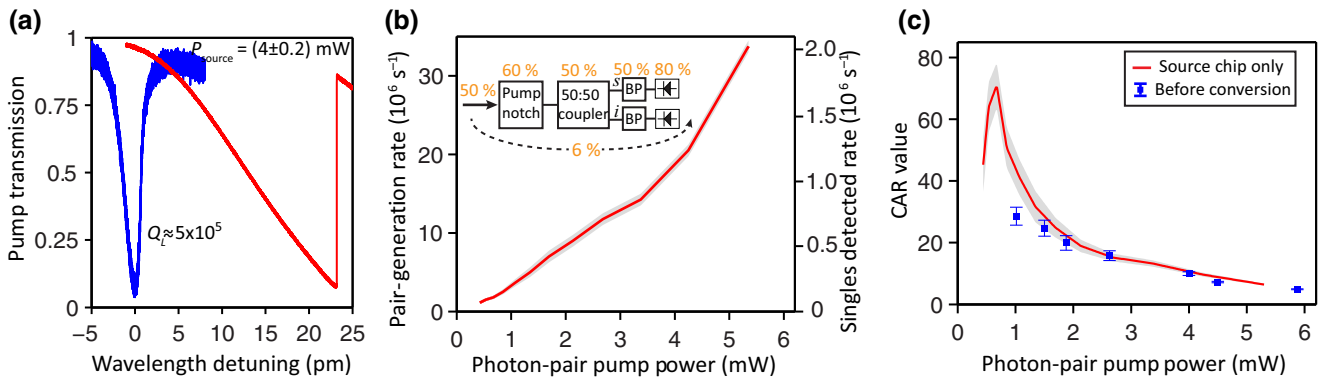


FIG. 6. Photon-pair-source characterization. (a) Transmission of the pump resonance in the linear case (blue curve) and at a pump power near 4 mW (red curve). (b) Detected signal (or idler) photon flux of the third-order pair (right y axis) and the inferred on-chip pair generation rate (left y axis) after accounting for transmission losses. The red solid line denotes the mean value of the photon flux and the gray area denotes the standard deviation extracted from the measured counts. The inset shows the experimental schematic and the transmission of relevant components is provided, including: waveguide outcoupling (50%), pump notch filter (60%), 50:50 coupler to split photons to two channels for coincidence measurement (50%), bandpass filters to select the desired signal and idler (50%), and the superconducting single-photon detectors (80% detection efficiency). Overall, approximately 6% of the photons emitted from the on-chip waveguide are detected. (c) The red solid line denotes the measured CAR for the photon-pair-source chip based on the experimental schematic shown in (b), with the gray area denoting the standard deviation extracted from the measured counts. We also plot the measured CAR values when the signal is passively transmitted through the frequency converter (i.e., no frequency conversion), corresponding to “before conversion” case shown in Fig. 3(e) in the main text.

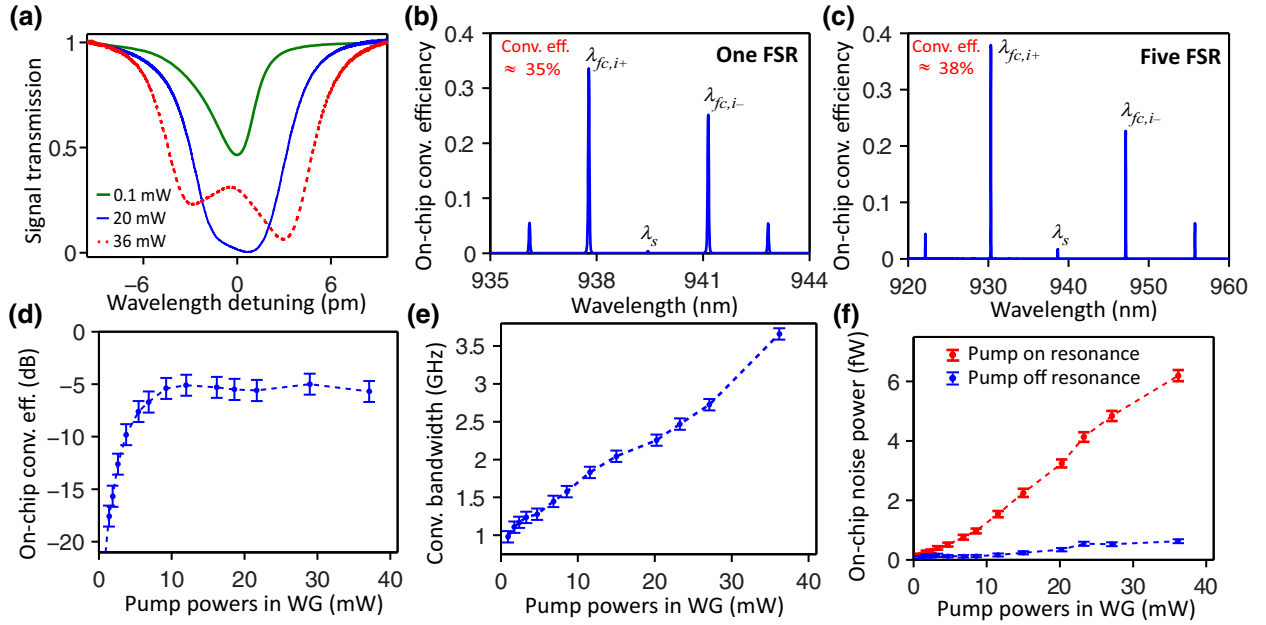


FIG. 7. Characterization of the microresonator frequency converter. (a) Signal transmission based on a swept tunable laser for several different pump powers. (b) Output spectrum of the frequency converter with one-FSR separation between the two pump lasers (frequency translation approximately equal to 572 GHz) for a total pump power of 20 mW on chip (10 mW each). The power in the 930-nm band is normalized by the input signal power, corresponding to the on-chip conversion efficiency. (c) Frequency-conversion spectrum for five-FSR separation between two pump lasers (frequency translation approximately equal to 2.86 THz) for a total pump power of 20 mW on chip (10 mW each). The next three figures show the dependence on total on-chip pump power of the (d), on-chip conversion efficiency of the blue-shifted idler $f_{c,i+}$, (e) conversion bandwidth, and (f), on-chip noise. Error bars in (d),(f) represent one standard deviation values caused by fluctuations in the detected signal.

the conversion bandwidth and the noise associated with the FWM BS process also increase with the pump power. This noise is believed to stem from fluorescence centers in the Si_3N_4 material. It is much stronger when the pumps are aligned with their respective cavity modes, a consequence of the resonance enhancement of the pump intensities. The optimal choice of pump power depends on the experiment, where the input signal bandwidth, input signal flux, and desired signal-to-noise level for the frequency-converted idler are taken into consideration.

2. Conversion efficiency versus signal input bandwidth

The photon-pair source used in the quantum frequency-conversion experiment differs from the cw laser used in the classical characterization in that the pair photons have a much larger bandwidth (640 vs 200 kHz). In this subsection, we investigate the impact of such a finite bandwidth on the conversion efficiency by employing a simplified set of coupled-mode equations developed in our earlier work [6]:

$$t_R \frac{dE_s}{dt} = -(\alpha + i\delta_s)E_s + i\Omega_0 E_{i-} + i\Omega_0 E_{i+} + i\sqrt{\theta P_s}, \quad (\text{C1})$$

$$t_R \frac{dE_{i+}}{dt} = -[\alpha + i(\delta_s + \Omega_1 + \Omega_2)]E_{i+} + i\Omega_0 E_s, \quad (\text{C2})$$

$$t_R \frac{dE_{i-}}{dt} = -[\alpha + i(\delta_s - \Omega_1 + \Omega_2)]E_{i-} + i\Omega_0 E_s, \quad (\text{C3})$$

where $E_{s,i\pm}$ are the intracavity mean fields corresponding to the signal and two adjacent idlers ($|E|^2$ representing the average power traveling inside the cavity), t_R is the round-trip time, α is the cavity loss rate in the 930-nm band [$\alpha = \hat{\omega}_s t_R / (2Q_L)$ with $\hat{\omega}_s$ and Q_L being the signal resonance frequency and its loaded Q , respectively], δ_s denotes the signal detuning, θ is the power coupling coefficient between the resonator and the access waveguide ($\theta = \hat{\omega}_s t_R / Q_c$ with Q_c being the coupling Q), and P_s represents the power of a cw signal. The parameters Ω_n ($n = 0, 1, 2$) are defined as

$$\Omega_0 \equiv 2\gamma_s L |E_{p1} E_{p2}|, \quad (\text{C4})$$

$$\Omega_1 \equiv \frac{\delta_{i+} - \delta_{i-}}{2}, \quad (\text{C5})$$

$$\Omega_2 \equiv \frac{\delta_{i+} + \delta_{i-} - 2\delta_s}{2}, \quad (\text{C6})$$

where γ_s is the Kerr nonlinear coefficient in the 930-nm band, L is circumference of the microring resonator

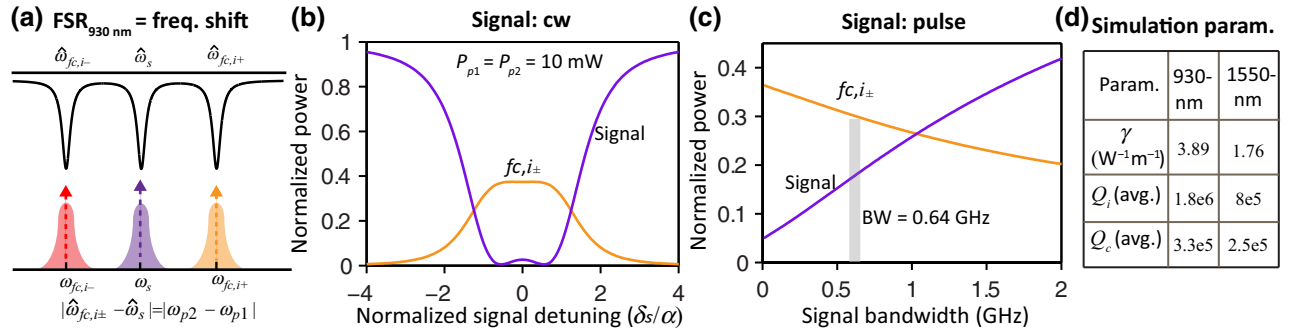


FIG. 8. Conversion efficiency versus signal bandwidth. (a) Schematic illustrating the condition for symmetric idlers: the FSR in the 930-nm band equals the frequency shift set by the two pump lasers in the 1550-nm band. (b) Conversion efficiencies (orange) of the two idlers (equal in this case) and normalized transmission of the signal (purple) as a function of the signal detuning. (c) Conversion efficiencies (orange) of the two idlers (equal in this case) and normalized transmission of the signal as a function of its input bandwidth at zero signal detuning. The gray bar highlights the 640-MHz bandwidth for the pair source used in this work. (d) Table listing simulation parameters, including the nonlinear coefficient (γ), the intrinsic quality factor (Q_i), and the coupling quality factor (Q_c) in both the 930- and 1550-nm bands. The pump power is assumed to be 20 mW in the 1550-nm band (10 mW for each pump).

($L \equiv 2\pi R$ with R being the ring radius), $E_{p1,p2}$ denote the intracavity mean fields of the two pumps in the 1550-nm band, and $\delta_{i\pm}$ are the detunings of the two idlers. A straightforward calculation shows that $\Omega_{1,2}$ can be expressed as

$$\Omega_1 \approx (D_1|\mu| - |\omega_{p1} - \omega_{p2}|) t_R - \frac{\gamma_p L}{2} (|E_{p1}|^2 - |E_{p2}|^2), \quad (C7)$$

$$\Omega_2 \approx \frac{1}{2} D_2 \mu^2 t_R, \quad (C8)$$

where γ_p is the Kerr nonlinear coefficient in the 1550-nm band.

It is obvious from Eqs. (C1)–(C3) that the two idlers are symmetric if $\Omega_1 = 0$. In our configuration, the two pumps usually have equal power. Thus, according to Eq. (C7), Ω_1 is determined by the difference between the frequency shift, which is dictated by the frequency difference of the two pump lasers ($|\omega_{p1} - \omega_{p2}|$), and the FSR in the 930-nm band (D_1). For simplicity, here we limit our discussion to the one-FSR case and consider the matched scenario first [Fig. 8(a)]. Figure 8(b) shows the simulated result for the cw case, where the signal is almost depleted (transmission less than 5%) and each idler has a conversion efficiency around 38%. Next, we extend the analysis to the finite bandwidth pulse by expanding its spectrum into a series of single-frequency inputs (i.e., a Fourier expansion). As can be seen in Fig. 8(c), the conversion efficiency of the frequency converter gradually decreases with the increased bandwidth, whereas the signal transmission steadily increases. For example, for an input bandwidth of 0.64 GHz, which corresponds to the case of the photon-pair source, the conversion efficiency degrades from 38 to 30%, while the signal transmission increases from 5%

to approximately 16%. Further increasing the input bandwidth beyond 1 GHz results in the signal being stronger than the two idlers, a clear indication that the signal cannot be sufficiently depleted.

3. Asymmetric conversion efficiencies between two idlers

In this subsection, we consider the scenario that the frequency shift (set by the difference in pump frequencies) is not equal to the FSR in the 930-nm band. We again limit our discussion to the one-FSR case as illustrated in Fig. 9(a). In this case, the lack of symmetry in the frequency detunings of the two idlers (i.e., $\Omega_1 \neq 0$) results in different conversion efficiencies for a given signal detuning. For example, Fig. 9(b) plots the simulation results corresponding to the case of a cw signal, where the maximum achievable conversion efficiency for the blue or red idler is slightly higher (around 46%) than the symmetric case (38%), due to the suppression of the other idler at that level of detuning. Similarly, for a pulsed input with a finite bandwidth [Fig. 9(c)], we can adjust the relative strength between the blue and red idlers by varying the signal detuning, a feature that is used in our experiment to increase the efficiency of the targeted idler.

We note that our use of a simplified coupled-mode theory results in overestimates of the conversion efficiency in comparison to a full theory, which takes into account the higher-order idler generation as described in the previous section. As discussed in Ref. [6], quantitative agreement between theory and experiment can be achieved by including a larger basis of frequency modes, e.g., through adaptation of the mean-field Lugiato-Lefever equation (LLE) that is used in the modeling of microresonator frequency combs [39,40].

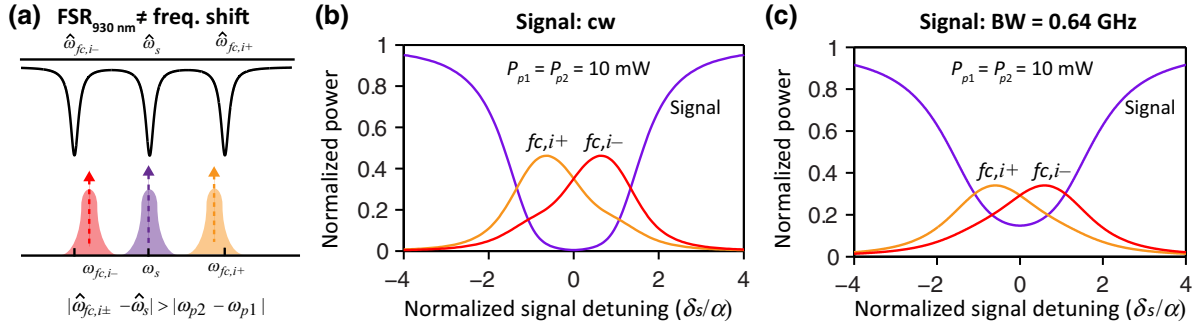


FIG. 9. Asymmetric conversion efficiencies in two idlers. (a) Schematic illustrating asymmetric idlers: the FSR in the 930-nm band is not equal to the amount of frequency translation set by the two 1550-nm pumps. (b) Conversion efficiencies of the two idlers (orange and red) and normalized transmission of signal (purple) as a function of the signal detuning for $\Omega_1 = 0.5\alpha$, with other simulation parameters being the same as listed in Fig. 8(d). (c) Conversion efficiencies of the two idlers (orange and red) and normalized transmission of the signal (purple) for an input bandwidth of 0.64 GHz.

APPENDIX D: QFC EXPERIMENTAL SETUP

The measurements performed in Figs. 2 and 3 are based on the same experimental schematic shown in Fig. 10, except that the two 1550-nm pumps for the frequency conversion are off in Fig. 2 (before conversion) and on in Fig. 3 (after conversion). The coupling efficiency between the lensed fiber and the photonic chip is 50 to 60% per facet by implementing inverse tapers at the ends of the waveguide. The overall transmission of the signal (idler) from the photon-pair chip to the single-photon detector is approximately 1.7% (0.72%), which is estimated by multiplying the transmission of various components in the optical path. For example, for the signal we have outcoupling of the photon-pair chip (50%), pump notch filter (60%), wavelength division multiplexer (WDM) to separate into two channels (90%), signal bandpass filter (50%), 1550- and 930-nm WDM to combine signal in the 930-nm band and two pumps in the 1550-nm band (80%), frequency-converter chip (50% per facet), another 1550- and 930-nm WDM to separate light to the 1550- and 930-nm bands (80%), and superconducting nanowire single-photon detectors (SNSPD, 80% detection efficiency), totaling to 1.73%. Similarly, the overall transmission for the idler can be calculated (0.72%), noting that the 10% port of the WDM has an actual transmission of 6% instead of 10%. The photon count rate shown in the left y axis in Figs. 2(b) and 3(a), 3(d), 3(f) corresponds to the detected photon flux. Error bars are one standard deviation values and stem from fluctuations in the detected flux.

APPENDIX E: NOISE ANALYSIS FOR QUANTUM FREQUENCY-CONVERSION EXPERIMENT

In this section, we present a detailed analysis of noise in the quantum frequency-conversion experiment. Specifically, we study the noise before frequency conversion

(Appendix E.1), how it changes after frequency conversion (Appendix E.2), its impact on the CAR measurement (Appendix E.3), and future directions for reducing noise (Appendix E.4).

1. Noise before frequency conversion

As illustrated in Fig. 11(a), there is a broadband background noise associated with the photon pairs generated in the first microring. This noise arises from Raman scattering induced by the pump during its propagation in the optical fiber that connects the laser to the photonic chip. Despite the use of multiple bandpass filters in the experiment, a complete suppression of the Raman noise is challenging due to the relatively small spectral separation between the selected photon pair and the pump. As a result, the SNR before conversion, which is defined as the ratio between the signal and the background noise at the input of the frequency converter, is limited. This SNR can be experimentally measured by comparing the photon counts in the relevant photon pair signal and idler frequency bins between when the pump is off resonance with its relevant cavity mode (Raman noise only in the signal and idler bins) and the pump on-resonance case (Raman and photon pairs), and noting that Raman noise entering the chip is the same in these two cases. For example, the SNR for the pump power near 4 mW [corresponding to the spectrum shown in Fig. 2(b) in the main text] is estimated to be around 2.5, indicating that a significant portion of the detected photon flux is Raman noise (29% at this power level). The presence of the Raman noise also explains the power dependence of the detected photon rates being different than quadratic. In fact, by decomposing the photon counts into the Raman noise and the photon pairs, with the former having a linear power dependence and the latter having a quadratic dependence, a reasonable agreement between theory and experiment is achieved in Fig. 11(b).

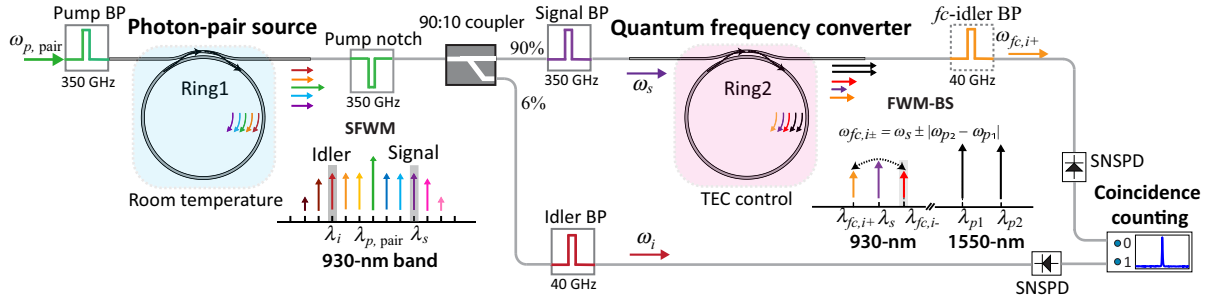


FIG. 10. Experimental schematic for QFC. After selecting a specific set of signal and idler frequency bins from the photon-pair source, the signal is combined with two 1550-nm pumps using a 930-nm and 1550-nm WDM (not shown) and coupled to the frequency converter, with the idler directly transmitted to the detector. At the output of the frequency converter, light is separated into its respective frequency domains using another WDM (not shown) and the frequency-converted blue idler is filtered for coincidence measurement. BP, bandpass filter; SNSPD, superconducting single-photon detector; and TEC, thermoelectric controller.

We also plot the estimated SNRs before conversion in Fig. 11(c) (blue circles), which display a linear dependence on the pump power.

2. Noise after frequency conversion

The noise at the idler frequency after conversion is composed of several parts: (1) input noise at the signal frequency that gets frequency converted to the idler channel; (2) residual input noise at the idler frequency (i.e., due to Raman); and (3) additional noise contributed by the frequency converter. Compared to the input noise, which is due to broadband Raman scattering and is spectrally distributed over the width of the bandpass filter used to select the frequency-converted idler channel (350-GHz bandwidth), the converted noise is significantly reduced since the conversion bandwidth (2 GHz) is much smaller than the bandpass filter bandwidth. In our experimental configuration, the total contribution of these two types of noise at the idler frequency amounts to approximately 20% of the input noise, while 25% of the photon-pair signal is converted to the idler (without including coupling losses). On the other hand, the additional noise from the frequency converter is independent of the input noise and is solely determined by the two pumps in the 1550-nm band. This analysis suggests that the SNR after the conversion can be slightly improved if the input photon flux is much larger than the additional noise from the frequency converter [Fig. 11(c), red circles]. On the other hand, if the input photon flux is comparable to the frequency-conversion noise, the SNR is expected to deteriorate after the frequency conversion. However, this would only happen when the on-chip pair-generation rate is much smaller than 1.5×10^4 pairs/s (3 fW) for the current device.

3. CAR versus noise

To study the impact of noise on the CAR measurement, we use a simplified model developed in Ref. [41] for the

coincidence detection rate:

$$C_p = \gamma_e \eta_s \eta_i \tau_b, \quad (\text{E1})$$

where γ_e is the on-chip pair-generation rate, η_s (η_i) represents the total loss for the signal (idler), and τ_b is the time-bin size. Similarly, the detection probability per unit time for the signal (or idler) is given by $p_{s,i} = \gamma_e \eta_{s,i} + dk_{s,i}$, where $dk_{s,i}$ denote the noise (including dark counts from detectors) associated with the signal and idler detection. If the photon flux is low enough, we can neglect the contribution from multiphoton generation, and the accidental coincidence detection rate is given by

$$C_a = (\gamma_e \eta_s + dk_s)(\gamma_e \eta_i + dk_i) \tau_b^2. \quad (\text{E2})$$

Using the definition of $\text{CAR} \equiv C_p/C_a$, we obtain the following expression after some simplification:

$$\text{CAR} = \frac{1}{\gamma_e \tau_b} \frac{1}{[1 + 1/(\text{SNR}_s)][1 + 1/(\text{SNR}_i)]}, \quad (\text{E3})$$

where $\text{SNR}_{s,i}$ represent the SNRs for the signal and idler. The dependence of CAR on pump power, as shown in Fig. 6(c), can be understood using Eq. (E3). For example, at high pump powers the term containing the SNR can be neglected (close to 1), and the CAR is inversely proportional to γ_e (until multiphoton contribution becomes significant). On the other hand, for small enough pump powers, the term containing SNR decreases much more rapidly than the reduced γ_e (mainly due to fixed dark counts from the detectors), hence leading to the peak observed in the CAR measurement. Equation (E3) also explains the insensitivity of CAR to the additional coupling loss [Fig. 6(c)], simply because the SNR is kept the same during the coupling process.

In the QFC experiment, the CAR values before and after frequency conversion are compared. Since the same

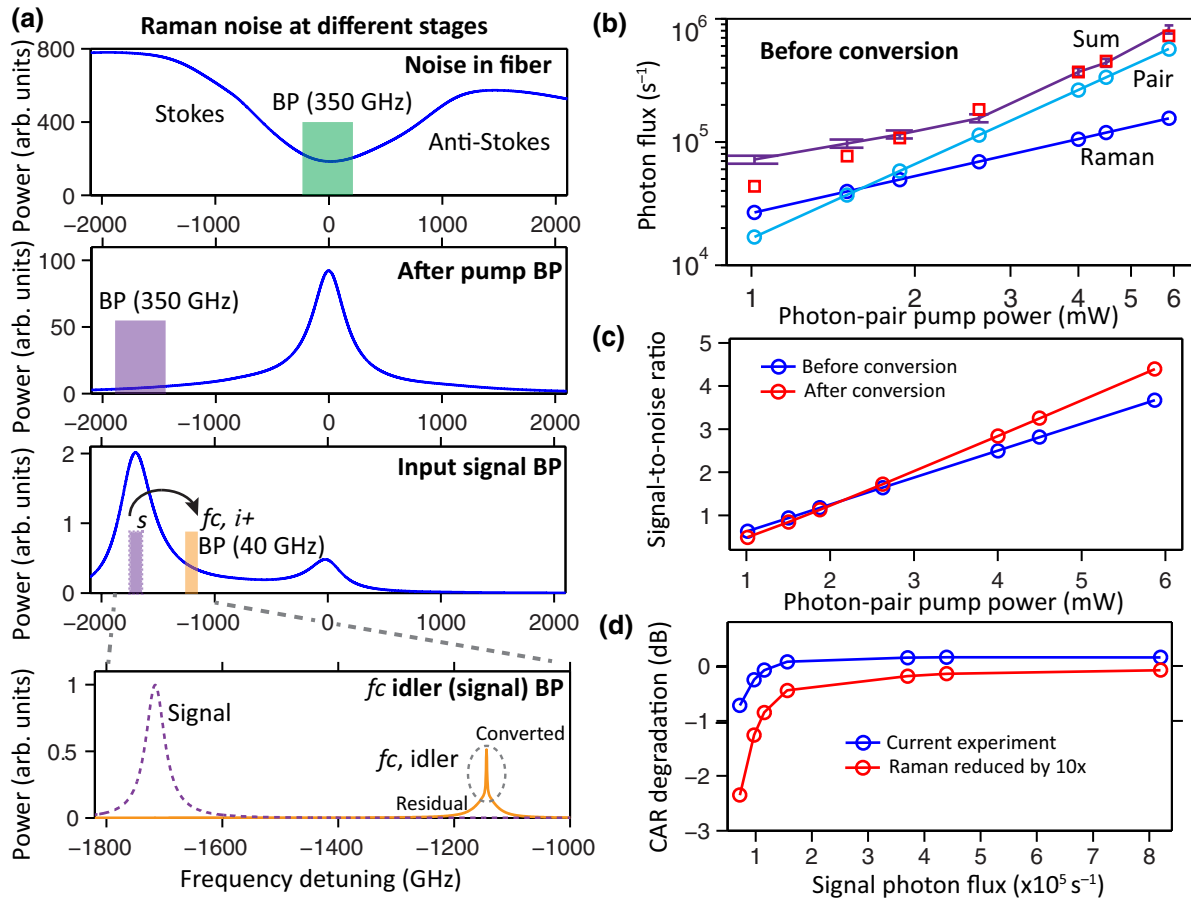


FIG. 11. Noise analysis for QFC. (a) Simulated Raman noise at various stages of the QFC experiment (counting from top to bottom): (1) in the optical fiber that connects the laser to the photon-pair chip, with the x axis being the frequency detuning relative to the pump frequency; (2) at the input of the photon-pair chip after a 350-GHz bandwidth bandpass filter (1 nm in wavelength, see Fig. 10) is spectrally aligned with the photon-pair-source signal frequency. The transmission of all the bandpass filters is taken to be 50%; (3) at the input of the frequency-converter chip after using a 350-GHz bandwidth bandpass filter to select the signal; and (4) at the idler frequency after using a 40-GHz bandwidth bandpass filter to select the frequency-converted blue idler, which consists of the frequency-converted part (sharp peak in the yellow solid curve) and the residual Raman noise from the input due to insufficient spectral suppression (wider base in the yellow solid curve). In comparison, we also plot the Raman noise at the signal frequency if we use a 40-GHz bandwidth bandpass filter to select the signal (violet dotted curve). (b) Decomposing the detected photon counts from the photon-pair source into Raman noise (blue circles) and photon pairs (cyan circles). Their sum (red squares) agrees with the experimental data reasonably well [violet line with error bars, also shown in Fig. 3(f) in the main text]. (c) Estimated SNR values before and after frequency conversion based on a conversion efficiency of 25% and the various noise contributions described in the text. (d) Degradation of CAR values for the QFC experiment shown in Fig. 3 in the main text (blue circles) as well as for a hypothetical scenario that the Raman noise on the input source is further suppressed by a factor of 10 through the use of narrower bandpass filters (red circles). The x axis corresponds to the signal photon flux in the “before conversion” case in (b), which would be the on-chip signal photon flux if there is no coupling loss.

photon-pair-source idler is used in both CAR measurements, we only need to focus on the change in SNR for the signal photons when they get mapped to frequency-converted idler photons. The degradation of the CAR can therefore be obtained as

$$\text{CAR}_{\text{degradation}} = \frac{1 + 1/(\text{SNR}_{s,\text{before}})}{1 + 1/(\text{SNR}_{s,\text{after}})}. \quad (\text{E4})$$

A straightforward calculation for the QFC experiment performed in this work shows that the CAR is expected to stay almost the same as the before conversion case [blue circles in Fig. 11(d)], agreeing with our experimental data. In addition, we also consider a hypothetical scenario in which the Raman noise is suppressed further by one order of magnitude. In this case, the Raman noise near the pump power of 1 mW becomes comparable to the additional noise from the frequency converter, leading to a more significant drop

in the CAR values after conversion [red circles in Fig. 11(d)]. Again, we want to stress here that the CAR values can be well maintained if the signal photon flux is large enough.

4. Steps for improved performance

The above analysis indicates that the input Raman noise within the photon-pair source currently limits the pair-source CAR values to around 30, and is significantly larger than the noise added by the frequency converter. As a result, we do not observe any significant degradation in CAR in the quantum frequency-conversion experiment. In this section, we consider steps that might improve the overall performance of the system.

We start with the frequency converter, noting that while its performance is suitable for the microresonator photon-pair source we develop in this work, reductions in added noise are needed if either the source brightness or input noise from the source (e.g., the Raman contribution) are reduced [Figs. 11(c) and 11(d)]. Low-loss, narrowband spectral filtering (at the GHz or few hundred MHz level) at the output of the frequency converter is an approach that is often used to reduce noise in QFC, for example, in several recent demonstrations of downconversion to the telecommunications band use periodically poled $\chi^{(2)}$ waveguides [17,22–24]. In this work, we use a 40-GHz bandpass filter after the QFC chip. However, we note that in contrast to all previous works on QFC, our device is resonator based, and hence it naturally acts a spectral filter itself, with a bandwidth set by the conversion bandwidth (about 2 GHz in the experiment we present). However, the configuration and extinction ratio of the converter is not optimized for filtering. Thus, an appealing approach would be to integrate an on-chip filter after the converter, and indeed, filters have been implemented in Si_3N_4 using both microring-based [28] and grating-based [42] geometries. The bandwidth of this filter depends on the source—a GHz-level bandwidth is appropriate for the current pair sources we work with, but for much narrower-band photons, e.g., from a quantum emitter with a long lifetime, more aggressive narrowband filtering should be employed. Considering that linewidths approximately equal to 10 MHz are achieved in Si_3N_4 microring resonators [43], there is significant scope for implementing narrower-band on-chip filters.

Ultimately, however, our frequency converter does add some amount of noise, which is resonant with the frequency-converted photons and hence cannot be readily removed through spectral filtering. It seems unlikely to be due to Raman scattering in the Si_3N_4 [44], given that our signal and idler photons are separated by 130 THz (and on the anti-Stokes side) of the 1550-nm pump. We tentatively hypothesize that the noise is due to fluorescence from the Si_3N_4 material, possibly due to nanocrystal formation during the film growth or annealing, which is known to be

sensitive to specific growth parameters [45]. Future studies of the influence film growth and annealing conditions on added noise are needed to help elucidate such points.

Additional spectral filtering is also needed to improve the performance of our photon-pair source. In particular, this would aim to further suppress the broadband Raman noise that enters into the photon-pair source and overlaps with its signal and idler frequency bins (as well as the converted frequency bin), as described in the previous section. Similar to the output spectral filtering described above, such an input filter (i.e., placed before the photon-pair source) could be implemented on chip.

Finally, cryogenic temperatures are known to significantly reduce Raman noise in optical fibers [46,47], and is thus a straightforward path to improving the performance of the photon-pair source (i.e., by limiting the noise entering the Si_3N_4 chip). The influence of cryogenic temperatures on the performance of the Si_3N_4 devices themselves (e.g., in terms of the added noise produced by the frequency converter) is unknown, but worth exploring. Furthermore, direct integration of SNSPDs with Si_3N_4 photonic circuits [30] requires cryogenic temperatures for operation.

APPENDIX F: HONG-OU-MANDEL (HOM) INTERFERENCE EXPERIMENTAL DETAILS

In the HOM interference experiment carried out in Fig. 4 we employ the same frequency converter that is used for the demonstration of quantum frequency conversion in Fig. 3, but replace the photon-pair source by another microring that has approximately the same FSR as the frequency converter (by simply choosing a different ring width). Tuning of the frequency converter's spectral translation range to ensure the precise spectral matching needed for HOM interference is achieved by varying the frequency difference of the two pump lasers that drive the frequency-conversion process. While this pump frequency difference sets the spectral translation range, the efficiency of the process depends on the pump powers coupled into the resonator, which in turn depend on the detuning of each pump with respect to its cavity mode. When using multiple strong pumps, a challenge is in simultaneously setting the detuning of both pumps at desired values, as adjustment of one pump frequency influences the detuning of the other, due to the thermo-optic effect (i.e., changes in the in-coupled pump power influence the location of all of the cavity modes). Typically, an iterative procedure is required, and this is what has been employed in all experiments in which the pump frequencies are not varied.

In the HOM interference experiments, we need to actively vary the pump frequency separation. To avoid having to implement the iterative approach for every desired frequency separation value, we instead take advantage of the fact that FWM BS efficiency depends on

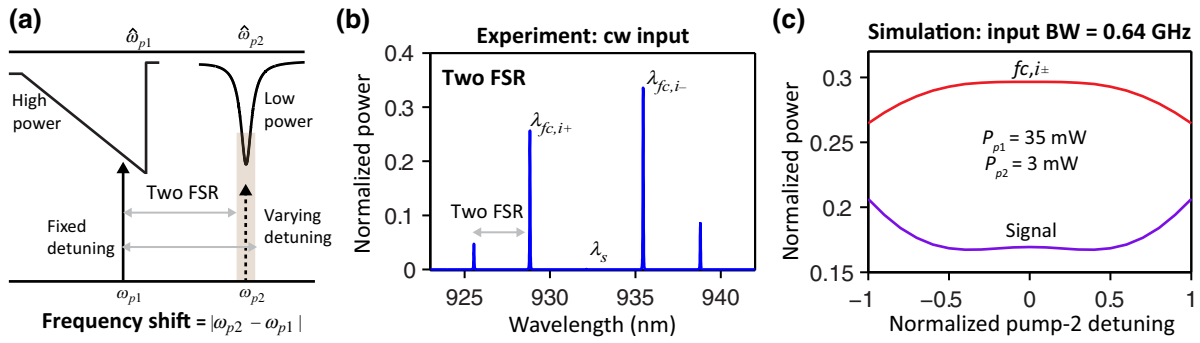


FIG. 12. Frequency shift tuning by pump lasers. (a) Experimental configuration for tuning the frequency shift between the signal and idlers in the 930-nm band by varying the frequency detuning of pump lasers in the 1550-nm band: pump 1 is set at a much higher power than pump 2, so that the pump-1 cavity resonance exhibits thermal bistability while the pump-2 cavity resonance resides in the linear regime. By fixing the detuning of pump 1 while varying the detuning of pump 2, we can thus tune the spectral translation range of our frequency converter without modifying its thermal dynamics. (b) Experimental frequency-conversion spectrum following this approach, with the pump frequency separation of about two FSRs (approximately equal to 1.14 THz), and using a cw 930-nm band input signal. The optical spectrum is normalized by the signal input power, showing a conversion efficiency near 34% for the red idler. (c) Simulated conversion efficiencies for a pulsed signal input (bandwidth around 0.64 GHz) as a function of the pump-2 laser detuning. Here we assume the signal detuning is fixed at zero, and the frequency shift is equal to two FSRs in the 930-nm band when the pump-2 laser is set at zero detuning. The x axis is normalized by half of the cavity linewidth (0.5 GHz).

the product of the two pump powers. This means that low power in one pump can be largely compensated by increasing the power in the second pump. The approach is illustrated in Fig. 12(a). We set one pump (pump 2) at a low enough power so that its cavity resonance stays in the linear regime, whereas the other pump (pump 1) is set at a high enough power to provide the desired conversion efficiency. In this configuration, the thermal dynamics of the microresonator is dominated by the strong pump (pump 1 with fixed laser detuning) and is almost independent of the detuning of the weak pump 2. This allows us to freely adjust the detuning of pump 2 (either blue or red detuned with respect to its cavity resonance) without affecting the detuning of pump 1 with respect to its resonance. Figure 12(b) shows the output converted spectrum of a classical cw laser input, in the case where the pump frequency separation is approximately two FSRs,

and indicates that conversion efficiency $> 30\%$ can be achieved. Figure 12(c) presents the results of a simulation (this time using a pulsed input source with linewidth of 640 MHz), showing that the peak conversion efficiency is largely maintained as the frequency of pump 2 (the low power pump) is varied on the order of the cavity linewidth.

Figure 13(a) shows the spectrum of the photon-pair source used in the HOM interference experiment, where the first-order pair is chosen as the signal and idler. The spectrum after conversion is plotted in Fig. 13(b), and the conversion efficiency of the red idler is estimated to be around $23\% \pm 3\%$. Moreover, we measure the self-correlation of the idler (or the frequency-converted red idler) using the experimental schematic shown in Fig. 5, by leaving one input arm of the 50:50 coupler open. The measured CAR value [Fig. 13(c)] around 2 meets the expectation for such probabilistic photon sources.

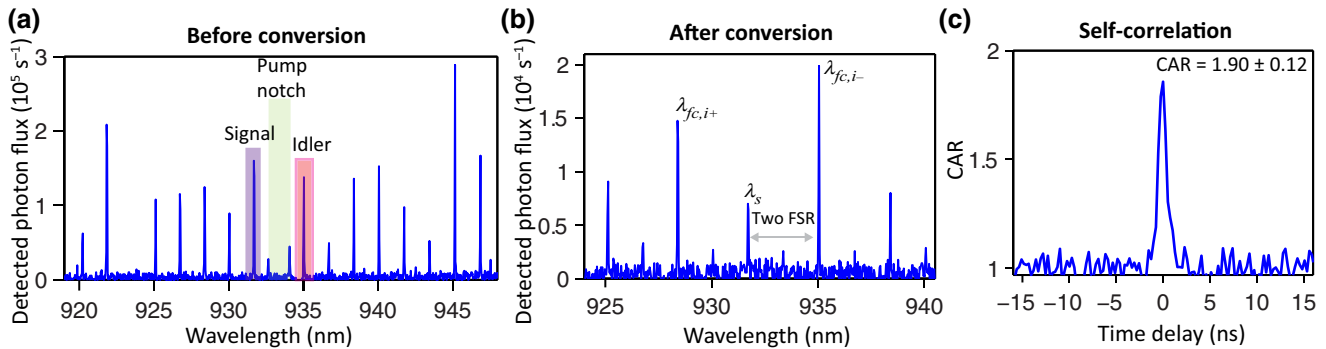


FIG. 13. Additional experimental data for two-photon interference. (a) Spectrum of the photon-pair source used in the two-photon interference experiment in Fig. 5. (b) Spectrum after frequency conversion. (c) Self-correlation measurement of the pair-source idler (or frequency-converted idler) using the schematic shown in Fig. 4, with one input arm of the 50:50 coupler left open.

APPENDIX G: HONG-OU-MANDEL INTERFERENCE: THEORETICAL MODEL

Finally, in this section we provide a brief calculation of the coincidence rate in the Hong-Ou-Mandel interference experiment. Even though in our experiment it is the interference between the frequency-converted red idler (from the signal) and the original idler, here for convenience we call them signal and idler. Assuming 1, 2 are the two input ports and 3, 4 are the two output ports, the fields at the output of a 50:50 coupler (or beam splitter) can be expressed as

$$\hat{E}_3^+(t) = N_3 [\hat{a}_1(\tau_1)e^{-i\omega_1(t-\tau_1)} + i\hat{a}_2(\tau_2)e^{-i\omega_2(t-\tau_2)}], \quad (\text{G1})$$

$$\hat{E}_4^+(t) = N_4 [\hat{a}_2(\tau_2)e^{-i\omega_2(t-\tau_2)} + i\hat{a}_1(\tau_1)e^{-i\omega_1(t-\tau_1)}], \quad (\text{G2})$$

where \hat{a}_n ($n = 1, 2$) is the destruction operation for the i_{th} input, ω_n is the corresponding center frequency, τ_n is the traveling time for the n_{th} photon to reach detectors, and N_3 and N_4 are normalization parameters. The coincidence rate is given by

$$P_{34}(t, t + \tau) = \langle \mathbf{1} |_s \langle \mathbf{1} |_i \hat{E}_3^-(t) \hat{E}_4^-(t + \tau) \hat{E}_4^+(t + \tau) \hat{E}_3^+(t) | \mathbf{1} \rangle_i | \mathbf{1} \rangle_s. \quad (\text{G3})$$

Substituting Eqs. (G1) and (G2) into Eq. (G3) results

$$\begin{aligned} P_{34}(t, t + \tau) = & |N_3 N_4|^2 \left\{ \langle \mathbf{1} |_s \hat{a}_1^+(\tau_1) \hat{a}_1(\tau_1) | \mathbf{1} \rangle_s \cdot \langle \mathbf{1} |_i \hat{a}_2^+(\tau_2 + \tau) \hat{a}_2(\tau_2 + \tau) | \mathbf{1} \rangle_i \right. \\ & + \langle \mathbf{1} |_s \hat{a}_1^+(\tau_1 + \tau) \hat{a}_1(\tau_1 + \tau) | \mathbf{1} \rangle_s \cdot \langle \mathbf{1} |_i \hat{a}_2^+(\tau_2) \hat{a}_2(\tau_2) | \mathbf{1} \rangle_i \\ & - \langle \mathbf{1} |_i \hat{a}_2^+(\tau_2 + \tau) \hat{a}_1(\tau_1 + \tau) | \mathbf{1} \rangle_s \cdot \langle \mathbf{1} |_s \hat{a}_1^+(\tau_1) \hat{a}_2(\tau_2) | \mathbf{1} \rangle_i e^{-i\Delta\omega_{12}\tau} \\ & \left. - \langle \mathbf{1} |_i \hat{a}_2^+(\tau_2) \hat{a}_1(\tau_1) | \mathbf{1} \rangle_s \cdot \langle \mathbf{1} |_s \hat{a}_1^+(\tau_1 + \tau) \hat{a}_2(\tau_2 + \tau) | \mathbf{1} \rangle_i e^{i\Delta\omega_{12}\tau} \right\}, \quad (\text{G4}) \end{aligned}$$

where $\Delta\omega_{12} \equiv \omega_1 - \omega_2$ is the frequency difference of the two input photons.

Equation (G4) has four components essentially describing the temporal correlations between the signal and idler photons: the first two terms describe the coincidence rate as if they are directly detected, and the last two terms describe the interference between them. These expressions can be computed based on the fact that, the signal and idler photons are created at the same time inside the microring, but they can couple out to the waveguide at different times with probability exponentially decaying with their time separation [i.e., $\exp(-\gamma|t_{\text{sep}}|)$ with γ being the photon decay rate]. As a result, we have

$$P_{34}(t, t + \tau) = \text{const} \times \left\{ e^{-\gamma|\tau - \Delta t_{12}|} + e^{-\gamma|\tau + \Delta t_{12}|} - 2e^{-\gamma|\tau|} \cos(\Delta\omega_{12}\tau) (\hat{\mathbf{e}}_s \cdot \hat{\mathbf{e}}_i)^2 \right\}, \quad (\text{G5})$$

where $\Delta t_{12} \equiv \tau_1 - \tau_2$ is the arrival time difference between the two photons, and $\hat{\mathbf{e}}_s$ ($\hat{\mathbf{e}}_i$) is the unit polarization vector for the signal (idler) photon.

The above equation allows us to obtain theoretical predictions for the two-photon interference experiment performed in Fig. 4 in the main text. For example, for the case that the two photons arrive at the 50:50 coupler at the same time ($\Delta t_{12} = 0$) with different frequencies, we have

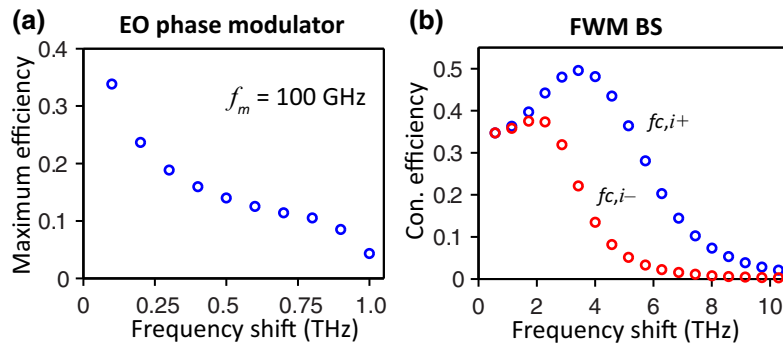
$$P_{34}^\perp(t, t + \tau) = \text{const} \times 2e^{-\gamma|\tau|} \quad (\text{orthogonal polarization}), \quad (\text{G6})$$

$$P_{34}^\parallel(t, t + \tau) = \text{const} \times 2e^{-\gamma|\tau|} [1 - \cos(\Delta\omega_{12}\tau)] \quad (\text{parallel polarization}). \quad (\text{G7})$$

Similarly, for photons arriving at the 50:50 coupler with a delay with respect to each other but with the same frequency, we have

$$P_{34}^\perp(t, t + \tau) = \text{const} \times (e^{-\gamma|\tau - \Delta t_{12}|} + e^{-\gamma|\tau + \Delta t_{12}|}) \quad (\text{orthogonal polarization}), \quad (\text{G8})$$

$$P_{34}^\parallel(t, t + \tau) = \text{const} \times (e^{-\gamma|\tau - \Delta t_{12}|} + e^{-\gamma|\tau + \Delta t_{12}|} - 2e^{-\gamma|\tau|}) \quad (\text{parallel polarization}). \quad (\text{G9})$$



The visibility plotted in Fig. 4(d) in the main text is defined as the contrast of coincidence peaks between the parallel and orthogonal polarizations:

$$\text{Visibility} \equiv \frac{P_{34,\max}^{\perp} - P_{34,\max}^{\parallel}}{P_{34,\max}^{\perp} + P_{34,\max}^{\parallel}}. \quad (\text{G10})$$

APPENDIX H: COMPARISON OF ELECTRO-OPTIC PHASE MODULATOR AND FWM BS APPROACHES

Here we briefly compare the performance of an electro-optic (EO) phase modulator and the FWM BS process for the frequency translation of optical signals. First, an optical carrier signal going through an EO phase modulator can be expressed in the following form:

$$E_m(t) = E_0 \sum_n J_n(\phi_0) \cos[(2\pi f_0 + n2\pi f_m)t], \quad (\text{H1})$$

where E_0 is a constant, $J_n(\phi_0)$ denotes the Bessel function of the first kind and of order n (n is an integer and ϕ_0 is the modulation depth), f_0 is the carrier frequency, and f_m is the modulation frequency. According to Eq. (H1), the normalized power at the n th sideband is simply given by $J_n^2(\phi_0)$, whose peak value by varying ϕ_0 corresponds to the maximum possible efficiency for a frequency translation of nf_m [Fig. 14(a)]. While the conversion efficiency for the first few sidebands can be decent (approximately equal to 10%–35%), it drops quickly below 10% at higher-order sidebands. Typically, f_m is limited to 100 GHz by the available electronic bandwidth, therefore rendering efficient frequency translation beyond 1 THz difficult.

On the other hand, in the FWM BS process, the conversion efficiency is determined by the frequency matching condition and the process can be efficient over a broad range. For example, Fig. 14(b) plots the expected conversion efficiency for the intraband frequency conversion when there is D_1 matching between the 1550- and 930-nm bands (i.e., as in our demonstrated devices). The blue idler maintains a high conversion efficiency ($> 30\%$) for a more than 5-THz-wide spectral window. A reduction in second-order (D_2) and higher-order dispersion terms can

FIG. 14. Comparison between the phase modulator and the FWM BS process. (a) Maximum possible efficiency for different sidebands in an electric-optic phase modulator with $f_m = 100$ GHz. (b) Simulated conversion efficiency for a 40- μm radius Si_3N_4 microring with matched FSR between the 1550- and 930-nm bands. In the simulation, we use $D_2/2\pi = -23.3$ MHz and $D_3/2\pi = -1.07$ MHz for the 1550-nm band, and $D_2/2\pi = -16.5$ MHz and $D_3/2\pi = 0.78$ MHz for the 930 nm.

enable wider spectral translation ranges to be achieved. We can further improve the efficiency by reducing the intrinsic propagation loss of the microresonator, increasing the level of overcoupling, and engineering the dispersion to enhance one idler while suppressing the other.

- [1] J. M. Lukens and P. Lougovski, Frequency-encoded photonic qubits for scalable quantum information processing, *Optica* **4**, 8 (2017).
- [2] M. Kues, C. Reimer, P. Roztocky, L. R. Cortés, S. Sciara, B. Wetzel, Y. Zhang, A. Cino, S. T. Chu, B. E. Little, D. J. Moss, L. Caspani, J. Azaña, and R. Morandotti, On-chip generation of high-dimensional entangled quantum states and their coherent control, *Nature* **546**, 622 (2017).
- [3] P. Imany, J. A. Jaramillo-Villegas, O. D. Odele, K. Han, D. E. Leaird, J. M. Lukens, P. Lougovski, M. Qi, and A. M. Weiner, 50-GHz-spaced comb of high-dimensional frequency-bin entangled photons from an on-chip silicon nitride microresonator, *Opt. Express* **26**, 1825 (2018).
- [4] L. Caspani, C. Xiong, B. J. Eggleton, D. Bajoni, M. Liscidini, M. Galli, R. Morandotti, and D. J. Moss, Integrated sources of photon quantum states based on nonlinear optics, *Light Sci. Appl.* **6**, e17100 (2017).
- [5] C. McKinstrie, J. Harvey, S. Radic, and M. Raymer, Translation of quantum states by four-wave mixing in fibers, *Opt. Express* **13**, 9131 (2005).
- [6] Q. Li, M. Davanco, and K. Srinivasan, Efficient and low-noise single-photon-level frequency conversion interfaces using silicon nanophotonics, *Nat. Photonics* **10**, 406 (2016).
- [7] A. Singh, Q. Li, S. Liu, Y. Yu, X. Lu, C. Schneider, S. Höfling, J. Lawall, V. Verma, R. Mirin, S. W. Nam, J. Liu, and K. Srinivasan, Quantum frequency conversion of a quantum dot single-photon source on a nanophotonic chip, *Optica* **6**, 563 (2019).
- [8] L. Olislager, J. Cussey, A. T. Nguyen, P. Emplit, S. Massar, J.-M. Merolla, and K. P. Huy, Frequency-bin entangled photons, *Phys. Rev. A* **82**, 013804 (2010).
- [9] T. Legero, T. Wilk, M. Hennrich, G. Rempe, and A. Kuhn, Quantum Beat of Two Single Photons, *Phys. Rev. Lett.* **93**, 070503 (2004).
- [10] P. Kumar, Quantum frequency conversion, *Opt. Lett.* **15**, 1476 (1990).
- [11] M. G. Raymer and K. Srinivasan, Manipulating the color and shape of single photons, *Phys. Today* **65**, 32 (2012).

- [12] S. Tanzilli, W. Tittel, M. Halder, O. Alibart, P. Baldi, N. Gisin, and H. Zbinden, Aphotonic quantum information interface, *Nature* **437**, 116 (2005).
- [13] M. T. Rakher, L. Ma, O. Slattery, X. Tang, and K. Srinivasan, Quantum transduction of telecommunications-band single photons from a quantum dot by frequency upconversion, *Nat. Photonics* **4**, 786 (2010).
- [14] H. J. McGuinness, M. G. Raymer, C. J. McKinstrie, and S. Radic, Quantum Frequency Translation of Single-Photon States in a Photonic Crystal Fiber, *Phys. Rev. Lett.* **105**, 093604 (2010).
- [15] S. Zaske, A. Lenhard, C. A. Keßler, J. Kettler, C. Hepp, C. Arend, R. Albrecht, W.-M. Schulz, M. Jetter, P. Michler, and C. Becher, Visible-to-Telecom Quantum Frequency Conversion of Light from a Single Quantum Emitter, *Phys. Rev. Lett.* **109**, 147404 (2012).
- [16] S. Ates, I. Agha, A. Gulinatti, I. Rech, M. T. Rakher, A. Badolato, and K. Srinivasan, Two-Photon Interference Using Background-Free Quantum Frequency Conversion of Single Photons Emitted by an InAs Quantum Dot, *Phys. Rev. Lett.* **109**, 147405 (2012).
- [17] B. Albrecht, P. Farrera, X. Fernandez-Gonzalvo, M. Cristiani, and H. de Riedmatten, A waveguide frequency converter connecting rubidium-based quantum memories to the telecom C-band, *Nat. Commun.* **5**, 3376 (2014).
- [18] S. Clemmen, A. Farsi, S. Ramelow, and A. L. Gaeta, Ramsey Interference with Single Photons, *Phys. Rev. Lett.* **117**, 223601 (2016).
- [19] L. J. Wright, M. Karpiński, C. Söller, and B. J. Smith, Spectral Shearing of Quantum Light Pulses by Electro-Optic Phase Modulation, *Phys. Rev. Lett.* **118**, 023601 (2017).
- [20] H. Rutz, K.-H. Luo, H. Suche, and C. Silberhorn, Quantum Frequency Conversion between Infrared and Ultraviolet, *Phys. Rev. Appl.* **7**, 024021 (2017).
- [21] C. Joshi, A. Farsi, S. Clemmen, S. Ramelow, and A. L. Gaeta, Frequency multiplexing for quasi-deterministic heralded single-photon sources, *Nat. Commun.* **9**, 847 (2018).
- [22] T. Walker, K. Miyanishi, R. Ikuta, H. Takahashi, S. Vartabi Kashanian, Y. Tsujimoto, K. Hayasaka, T. Yamamoto, N. Imoto, and M. Keller, Long-Distance Single Photon Transmission from a Trapped Ion via Quantum Frequency Conversion, *Phys. Rev. Lett.* **120**, 203601 (2018).
- [23] N. Maring, D. Lago-Rivera, A. Lenhard, G. Heinze, and H. de Riedmatten, Quantum frequency conversion of memory-compatible single photons from 606 nm to the telecom C-band, *Optica* **5**, 507 (2018).
- [24] A. Dreau, A. Tcheborateva, A. E. Mahdaoui, C. Bonato, and R. Hanson, Quantum Frequency Conversion to Telecom of Single Photons from a Nitrogen-vacancy Center in Diamond, *Phys. Rev. Appl.* **9**, 064031 (2018).
- [25] J. D. Siverns, J. Hannegan, and Q. Quraishi, Neutral atom wavelength compatible 780 nm single photons from a trapped ion via quantum frequency conversion, arXiv:1801.01193.
- [26] J. H. Weber, B. Kambs, J. Kettler, S. Kern, J. Maisch, H. Vural, M. Jetter, S. L. Portalupi, C. Becher, and P. Michler, Two-photon interference in the telecom C-band after frequency conversion of photons from remote quantum emitters, *Nat. Nanotechnol.* **14**, 23 (2019).
- [27] D. J. Moss, R. Morandotti, A. L. Gaeta, and M. Lipson, New CMOS-compatible platforms based on silicon nitride and Hydex for nonlinear optics, *Nat. Photonics* **7**, 597 (2013).
- [28] T. Barwicz, M. A. Popovic, P. T. Rakich, M. R. Watts, H. A. Haus, E. P. Ippen, and H. I. Smith, Microring-resonator-based add-drop filters in SiN: Fabrication and analysis, *Opt. Express* **12**, 1437 (2004).
- [29] C. Xiong, X. Zhang, A. Mahendra, J. He, D.-Y. Choi, C. J. Chae, D. Marpaung, A. Leinse, R. G. Heideman, M. Hoekman, C. G. H. Roeloffzen, R. M. Oldenbeuving, P. W. L. van Dijk, C. Taddei, P. H. W. Leong, and B. J. Eggleton, Compact and reconfigurable silicon nitride time-bin entanglement circuit, *Optica* **2**, 724 (2015).
- [30] C. Schuck, W. H. P. Pernice, and H. X. Tang, NbTiN superconducting nanowire detectors for visible and telecom wavelengths single photon counting on Si₃N photonic circuits, *Appl. Phys. Lett.* **102**, 051101 (2013).
- [31] X. Xue, Y. Xuan, C. Wang, P.-H. Wang, Y. Liu, B. Niu, D. E. Leaird, M. Qi, and A. M. Weiner, Thermal tuning of Kerr frequency combs in silicon nitride microring resonators, *Opt. Express* **24**, 687 (2016).
- [32] X. Lu, Q. Li, D. A. Westly, G. Moille, A. Singh, V. Anant, and K. Srinivasan, Chip-integrated visible-telecom entangled photon pair source for quantum communication, *Nat. Phys.* **15**, 373 (2019).
- [33] M. Savanier, R. Kumar, and S. Mookherjea, Photon pair generation from compact silicon microring resonators using microwatt-level pump powers, *Opt. Express* **24**, 3313 (2016).
- [34] C. Reimer, L. Caspani, M. Clerici, M. Ferrera, M. Kues, M. Peccianti, A. Pasquazi, L. Razzari, B. E. Little, S. T. Chu, D. J. Moss, and R. Morandotti, Integrated frequency comb source of heralded single photons, *Opt. Express* **22**, 6535 (2014).
- [35] J. A. Jaramillo-Villegas, P. Imany, O. D. Odele, D. E. Leaird, Z.-Y. Ou, M. Qi, and A. M. Weiner, Persistent energy-time entanglement covering multiple resonances of an on-chip biphoton frequency comb, *Optica* **4**, 655 (2017).
- [36] C. K. Hong, Z. Y. Ou, and L. Mandel, Measurement of Subpicosecond Time Intervals between Two Photons by Interference, *Phys. Rev. Lett.* **59**, 2044 (1987).
- [37] T. Legero, T. Wilk, A. Kuhn, and G. Rempe, in *Advances in Atomic, Molecular, and Optical Physics* (Elsevier, 2006), Vol. 53, pp. 253–289.
- [38] H.-H. Lu, J. M. Lukens, N. A. Peters, O. D. Odele, D. E. Leaird, A. M. Weiner, and P. Lougovski, Electro-Optic Frequency Beam Splitters and Tritters for High-Fidelity Photonic Quantum Information Processing, *Phys. Rev. Lett.* **120**, 030502 (2018).
- [39] S. Coen, H. G. Randle, T. Sylvestre, and M. Erkintalo, Modeling of octave-spanning Kerr frequency combs using a generalized mean-field Lugiato-Lefever model, *Opt. Lett.* **38**, 37 (2013).
- [40] Y. K. Chembo and C. R. Menyuk, Spatiotemporal Lugiato-Lefever formalism for Kerr-comb generation in whispering-gallery-mode resonators, *Phys. Rev. A* **87**, 053852 (2013).

- [41] S. Clemmen, K. P. Huy, W. Bogaerts, R. G. Baets, P. Emplit, and S. Massar, Continuous wave photon pair generation in silicon-on-insulator waveguides and ring resonators, *Opt. Express* **17**, 16558 (2009).
- [42] T. Zhu, Y. Hu, P. Gatkine, S. Veilleux, J. Bland-Hawthorn, and M. Dagenais, Arbitrary on-chip optical filter using complex waveguide Bragg gratings, *Appl. Phys. Lett.* **108**, 101104 (2016).
- [43] X. Ji, F. A. S. Barbosa, S. P. Roberts, A. Dutt, J. Cardenas, Y. Okawachi, A. Bryant, A. L. Gaeta, and M. Lipson, Ultra-low-loss on-chip resonators with sub-milliwatt parametric oscillation threshold, *Optica* **4**, 619 (2017).
- [44] A. Dhakal, P. Wuytens, F. Peyskens, A. Z. Subramanian, N. Le Thomas, and R. Baets, Silicon-nitride waveguides for on-chip Raman spectroscopy, *Proc. SPIE* **9141**, 91411C (2014).
- [45] P. Basa, P. Petrik, M. Fried, L. Dobos, B. Pécz, and L. Tóth, Si nanocrystals in silicon nitride: An ellipsometric study using parametric semiconductor models, *Physica E* **38**, 76 (2007).
- [46] H. Takesue and K. Inoue, 1.5- μm band quantum-correlated photon pair generation in dispersion-shifted fiber: Suppression of noise photons by cooling fiber, *Opt. Express* **13**, 7832 (2005).
- [47] Q. Lin, F. Yaman, and G. P. Agrawal, Photon-pair generation in optical fibers through four-wave mixing: Role of Raman scattering and pump polarization, *Phys. Rev. A* **75**, 023803 (2007).